B. M. Howe
Institute for Hydromechanics,
University of Karlsruhe,
West Germany

A. J. Chambers
Department of Mechanical Engineering,
University of Newcastle, N.S.W.,
Australia
Mem. ASME

S. P. Klotz

T. K. Cheung

R. L. Street
Mem. ASME
Department of Civil Engineering,
Stanford University,
Calif. 94305

Comparison of Profiles and Fluxes of Heat and Momentum Above and Below an Air-Water Interface

The velocity and temperature fields on both sides of an air-water interface were examined experimentally in order to understand better the physical processes of momentum and heat transfer through the surface layers about the interface. An examination of temperature and velocity profiles plotted in "law-of-the-wall" coordinates leads to the conclusion that, both in the air and in the water, the mechanism of momentum transfer is affected by surface roughness changes, but the mechanism of heat transfer is not. In the water surface layer the velocity fluctuations due to the wave-related motions are of the same order as the purely turbulent motions. The turbulent components closely resemble those found in boundary layers over solid walls. The measured total energy flux from the interface agrees well with the measured single-phase, vertical heat transport through the water surface layer.

Introduction

The velocity and temperature fields on both sides of an air-water interface have been examined experimentally in order to understand better the physical processes related to momentum and heat transfer through a water surface layer and a mobile boundary. These data will be ultimately used to calibrate a numerical model which couples the air and water boundary layers across the interface.

Experimental Equipment and Measurements

Instantaneous measurements of the horizontal velocity, u, the vertical velocity, v, the temperature, θ, and the wave height, η, were made beneath the air-water interface in the Stanford Wind, Water-Wave Research Facility. They were obtained using, respectively, a laser Doppler anemometer (LDA), a fast response (5 Hz) thermistor, and a capacitance-type wave height gage. A traversing Pitot-static tube and thermistor were referenced against free-stream probes to obtain velocity and temperature profiles in the air. Free-stream humidity was monitored by means of wet and dry-bulb thermistor thermometers. The water surface temperature was measured with an infrared radiometer (PRT-5).

The Stanford Wind, Water-Wave Research Facility [1–3] is about 35 m long; the test section is approximately 20 m long, 0.9 m wide and 1.93 m high. The channel is filled with water to a depth of about 1 m, leaving a 1 m deep air flow section. Air flow is produced by drawing air through the test section with a fan at the downstream end of the channel. Honeycombs, a series of turning vanes in the inlet, a set of filters, and several small-mesh screens straighten and condition the air flow. In the water a "beach" is used at the downstream end of the channel to minimize wave reflections into the test section. The water in this facility is heated from below by electric heating cables to establish an appropriate water-air temperature difference for each experimental run. However, the heaters must be turned off during the runs; otherwise the heater-induced buoyant convection would dominate the water boundary layer. As a consequence, since the water is warmer than the air, the water body cools during an experimental run.

The basic experimental setup and procedure was outlined in Howe et al. [1], in which preliminary water measurements at a wind speed of 3 m/s are reported. For the measurements reported herein, profiles consisting of a nominal 20 points (with 10 min of data per point) were made both in the air and the water. The wind speeds U_∞ were between 1.5 and 15.5 m/s, and the nominal bulk-water/free-stream-air-temperature difference was 8°C. The measuring station was 13 m from the air inlet.

There were specific objectives for each data run at a given wind speed; accordingly, not all instruments were used in each run. For example, in one case 10 data runs were made in a group, with two runs made at each of 5 wind speeds (1.6 to 13.1 m/s). The objective was to establish the repeatability of the measurements and to document the velocity and temperature profiles in the water; hence, no humidity data were taken. The velocity and temperature profile data were used from this data set, while other runs were made to focus on the

Contributed by the Heat Transfer Division for publication in the JOURNAL OF HEAT TRANSFER. Manuscript received by the Heat Transfer Division July 27, 1981.

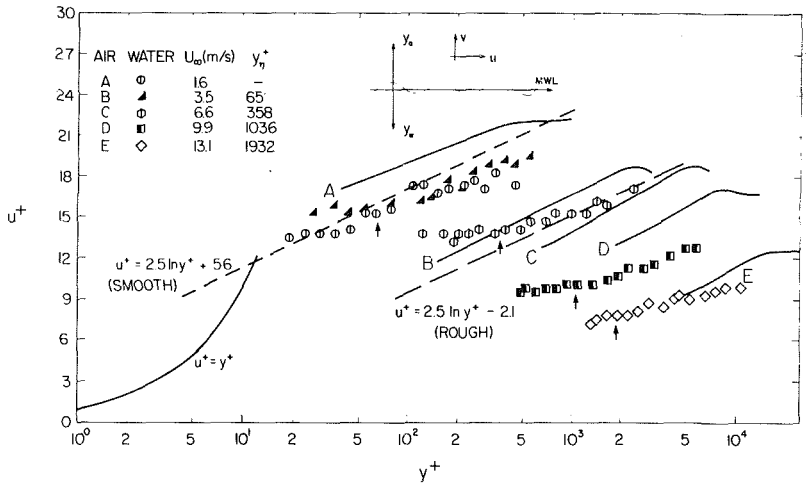

Fig. 1 Water and air velocity profiles in u^+, y^+ coordinates (y_η^+ values for each windspeed are shown by vertical arrows)

fluxes, and, in these cases, the free-stream humidity was measured so Stanton numbers could be computed.

The radiometer was calibrated in place after the method of Miller and Street [2]. Subsequent data analysis has indicated that the PRT-5 radiometer gave inconsistent results for $U_\infty = 9.9$ m/s. This is not significant for most results deduced herein. However, the law-of-the-wall temperature profiles require use of θ_s, the water-air interface temperature. Accordingly, as outlined below, we evaluated the variance in θ_s and developed a rational procedure to account for time-dependent trends in the data, reduce the impact of inherent uncertainties (see Appendix B where uncertainty estimates are given), and correct the 9.9 m/s data base.

Experimental Results

In what follows, u_s is the surface drift current, q is specific humidity in the air, and the subscripts a, w, s, ∞, and B refer, respectively, to air, water, the interface, the air free-stream, and the bulk water. In addition, u_* is the friction velocity, θ_* is the friction temperature, and η is the free surface displacement.

In Fig. 1, mean profiles of velocity in both the air and the water are plotted in "law-of-the-wall" coordinates (u^+ and y^+) for a range of wind speeds. As indicated on the insert, the coordinate y is the distance from the mean water level (MWL) into the air or the water, as appropriate. In the air, the appropriate normalizing quantities are u_{*_a} and ν_a, while for the water we use u_{*_w} and ν_w. To make the air and water plots comparable then, $u_a^+ = (\bar{u}_a - u_s)/u_{*_a}$ but $u_w^+ = (u_s - \bar{u}_w)/u_{*_w}$ (thus, both u^+ values approach zero as $y^+ \to 0$). Of course, $y_a^+ = u_{*_a} y_a/\nu_a$ and $y_w^+ = u_{*_w} y_w/\nu_w$. These data are from the 10 data runs mentioned above, in which two runs were made at each of 5 wind speeds. For clarity, only one profile is shown for each speed, and the air data are shown as a line because the air profile behavior is well known (see [3]). For the water data, we show actual data points. For the air profiles, u_* was determined using the profile technique ($\kappa = 0.40$), whereas for the water data, u_{*_w} was determined by a linear fit (with depth) of the direct measurements of the turbulent shear stress (discussed below) and extrapolation of the trend line to the interface. This procedure seemed to be the most consistent means of determining the interfacial stress and hence u_{*_w}. However, determination of u_{*_w} from u_{*_a} by stress continuity or from the single largest $\overline{u'v'}$ value in the direct measurement profile yields comparable results so the choice of method is not crucial. Also shown are the computed values of the waterwave boundary layer thickness, y_η^+, as

Nomenclature

c_p = specific heat
Q = a "heat" flux
q_* = friction humidity
St = a Stanton number $[= Q/\rho_w c_{p_w} U_\infty (\bar{\theta}_B - \bar{\theta}_\infty)]$
$S_{\eta\eta}$ = wave power spectrum
U_∞ = free stream air speed
u = horizontal velocity
u^+ = $(\bar{u}_a - u_s)/u_{*_a}$ or $(u_s - \bar{u}_w)/u_{*_w}$
u_* = friction velocity $[= (\overline{-u'v'})^{1/2}, (\tau_s/\rho)^{1/2}]$
v = vertical velocity
y = vertical coordinate measured as a distance away from the mean water level (y_a in the air; y_w in the water)
y^+ = $u_* y/\nu$
y_η = depth such that

$$\left(\int_0^{10} S_{\eta\eta}(f) e^{-2(2\pi f)^2 y_{\eta/g}} df\right) \Big/ \left(\int_0^{10} S_{\eta\eta}(f)\, df\right) = e^{-2}$$

θ = temperature
θ^+ = $(\bar{\theta}_w - \theta_s)/\theta_{*_w}$ or $(\bar{\theta}_a - \theta_s)/\theta_{*_a}$
η = wave height
θ_* = friction temperature $Q/\rho c_p u_* [= (\overline{v'\theta'})/u_*]$
κ = von Karman constant (0.40)
ρ = density
ν = kinematic viscosity

Superscripts

$\bar{}$ = time average
$'$ = turbulent component
$\tilde{}$ = wave component

Subscripts

a = air
B = bulk water
L = latent
R = radiative
S = sensible
s = surface
T = total
w = water
∞ = free stream air

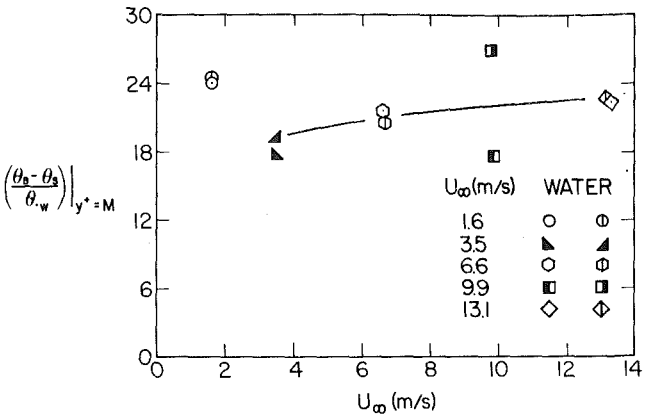

Fig. 2 Inverse Stanton number in water versus wind speed

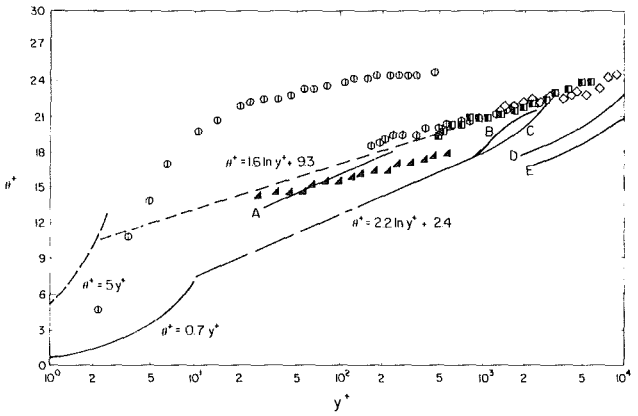

Fig. 3 Water and air temperature profiles in θ^+, y^+ coordinates (symbols same as in Fig. 1)

defined by Bye [4]. Here $y_\eta^+ = u_{*_w} y_\eta / \nu_w$, where y_η is the depth at which wave-associated fluctuations are reduced to e^{-1} times their mean water-level values and is computed as indicated in the nomenclature from the water wave power spectrum $S_{\eta\eta}$.

In Fig. 1, the slopes of the water velocity profiles are generally less than those in the air. Of particular interest is the apparent change in slope at the level of y_η^+ which occurs at all but the highest and lowest wind speeds. The wave effects are, of course, most pronounced for $y^+ < y_\eta^+$, and wave-induced mixing (as evidenced by an augmented eddy viscosity, see Csanady [5]) may well be responsible for the smaller velocity gradients. At the highest wind speed, wave breaking, as seen by heavy white capping, changes the near surface regime, and pronounced flattening of the profile is not evident. The relative interfacial roughness, as seen by the respective flows, is indicated by the vertical placement of the profiles on the plot. At the lowest wind speed (1.6 m/s) there are virtually no waves and the air profile seems to exhibit the "supersmooth" behavior discussed by Csanady [6]; the water profile does not.

The inherent uncertainty (± 0.1°C) in the radiometer-measured surface temperature θ_s causes significant scatter in plots in which water temperatures (determined by separate thermistor measurements) are differenced with θ_s because $\theta_w - \theta_s$ is always small. The air results are not significantly affected, because $\theta_B - \theta_s < 1°C$ while $\theta_s - \theta_\infty \simeq 8°C$. This effect was noticed because plots of $\theta_B - \theta_w$ show no significant variances compared to $\theta_w - \theta_s$ plots.

As noted above, the water temperature decreases during an experimental run, leading to a trend such that $\theta_B - \theta_\infty$ decreases with time. The decrease is more rapid at high wind speeds; however, the heat, mass, or momentum transport coefficients remain constant because U_∞ is held constant, and the rate of change of $\theta_B - \theta_\infty$ is such that the flow is essentially always in equilibrium. On the other hand, the magnitudes of the actual heat and mass transports do change; hence, profile and flux comparisons should account for this.

Our correction procedure for the water data (the above effects are not significant in the air for the reason that temperature differences are large) is as follows:

(*a*) The heat flux $\overline{v'\theta'}$ is taken to be the maximum value measured in the profile, and the depth of this measurement is noted as $y_w^+ = M$. Then $\theta_{*_w} = \overline{v'\theta'}/u_{*_w}$.

(*b*) The dimensionless number $(\theta_B - \theta_s)/\theta_{*_w}$ is plotted as a function of depth (essentially time because data were taken at sequentially increasing values of y_w) for each wind speed. Because the system time constant is very large (the total $\theta_B - \theta_s$ change occurs over several hours), the radiometer-induced scatter is removed by fitting a linear curve to the data and a "run or standard" inverse Stanton number $[(\theta_B - \theta_s)/\theta_{*_w}]$ is determined from the curve at $y^+ = M$.

(*c*) Finally, the time trend of heat transfer is removed by determining θ_w^+ as the product of a shape function and the "standard" inverse Stanton number for each run, viz.

$$\theta_w^+ = \frac{\theta_w(y) - \theta_s}{\theta_B - \theta_s} \left(\left[\frac{\theta_B - \theta_s}{\theta_{*_w}} \right]_{\text{at } y^+ = M} \right)$$

where θ_s and θ_B are those values determined at the time $\theta(y)$ was obtained.

Following step *b* above, Fig. 2 was plotted for all 10 data sets mentioned above. For all wind speeds except $U_\infty = 9.9$ m/s, the results of the two separate experiments are consistent and form a clear pattern. Accordingly, in Fig. 2,

(*a*) The dip at 3.5 m/s and the high values at 1.6 m/s are consistent with a change in surface conditions. Indeed, retrospective analysis of the air-flux measurements of McIntosh et al. [7] revealed precisely equivalent results for heat transfer in the air.

(*b*) The radiometer-induced errors at 9.9 m/s can be corrected either by taking the average of the two results or by using the trend value indicated by the solid curve (the result is the same!).

Figure 3 shows then the air and water temperature profiles in law-of-the wall coordinates. As McIntosh et al. [7] and Street et al. [3] reported, for $U_\infty > 2$ m/s, the air profiles cluster about the single correlation $\theta^+ = 2.2 \ln y^+ + 2.4$ and do not show significant effects of the increasing roughness with wind speed that the velocity profiles do. Surprisingly, the same is true for the water temperature profiles. The low speed case lies significantly above the rest of the data which fall on the correlation $\theta^+ = 1.6 \ln y^+ + 9.3$.

The slope of the water profiles indicates a turbulent Prandtl number of 0.63. This is in close agreement with 0.67 found by Ueda et al. [8] for open channel flow. The water profiles lie above the air profiles as expected because of Prandtl number dependence (see for instance Kader and Yaglom [9]). The profiles for the lowest wind speed case shift upwards and have intercepts comparable with those given by Kader and Yaglom [9] for smooth walls. Measurements in the water thermal sublayer agree roughly with $\theta^+ = \text{Pr}\, y^+$.

Representative normalized plots of the root-mean-square intensities of the velocity fluctuations in the water are contained in Figs. 4 and 5. (Again for clarity, here and in the following Figs. 6–9, only one of each of the pairs of data sets referred to above are plotted since the results are essentially identical.) Because we sought to examine water-wave effects, the vertical scale of the plots is the normalized depth, y/y_η. Wave-induced ($\tilde{u}$, $\tilde{v}$) and turbulent (u', v') components were separated by spectral means (see Appendix A1). Significantly, the wave-separation technique effectively collapses the

$$(\overline{\tilde{u}^2})^{1/2} \text{ and } (\overline{\tilde{v}^2})^{1/2}$$

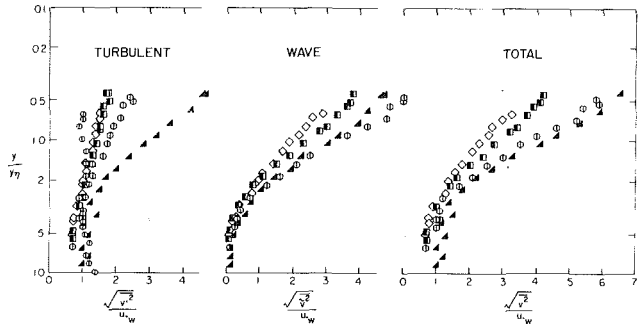

Fig. 4 Normalized root-mean-square vertical water velocity (symbols same as in Fig. 1)

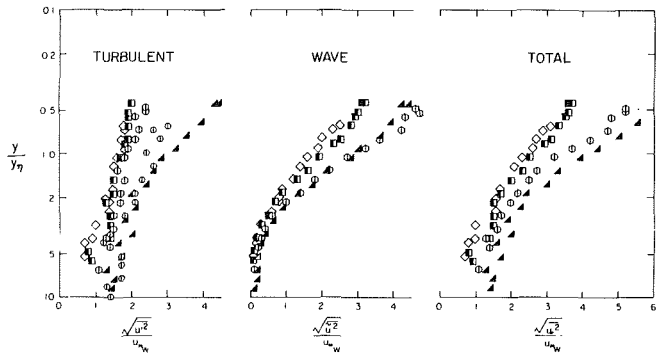

Fig. 5 Normalized root-mean-square horizontal water velocity (symbols same as in Fig. 1)

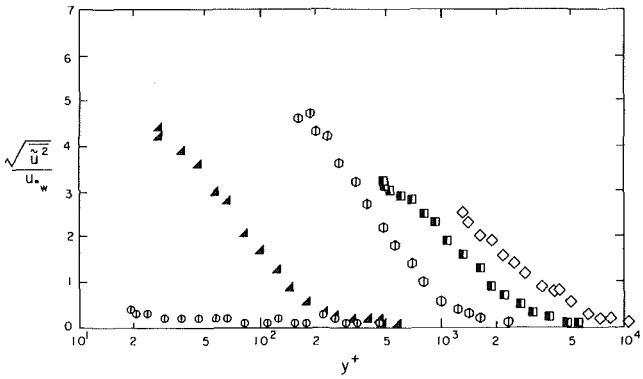

Fig. 6 Normalized root-mean-square horizontal, wave-induced velocity component versus y^+ (symbols same as in Fig. 1)

profiles. Although there is data scatter, there is no distinct trend with wind speed.

In all cases in which there are waves, for a given wind speed the figures show

$$(\tilde{v}^2)^{1/2} \gtrsim (\tilde{u}^2)^{1/2}, (\tilde{v}^2)^{1/2} \gtrsim (\tilde{u}^2)^{1/2}$$

and generally

$$(\overline{v'^2})^{1/2} \lesssim (\overline{u'^2})^{1/2}$$

Furthermore, each of the normalized horizontal and vertical components, when plotted versus y/y_η, decreases with increasing wind speed and appears to approach a single curve at the highest wind speeds when the waves become increasingly two-dimensional and when significant white-capping begins to occur.

Except very far from the interface ($y/y_\eta \gtrsim 3$), wave-induced ($\tilde{}$) and purely turbulent ($'$) fluctuations in both the horizontal and vertical at any given wind speed are roughly equal in magnitude. This observation points to the characteristic difference between fetch-limited laboratory flows and field (ocean) studies where the wave-induced components (associated with the dominant wave frequency) are typically much smaller than the purely turbulent components.

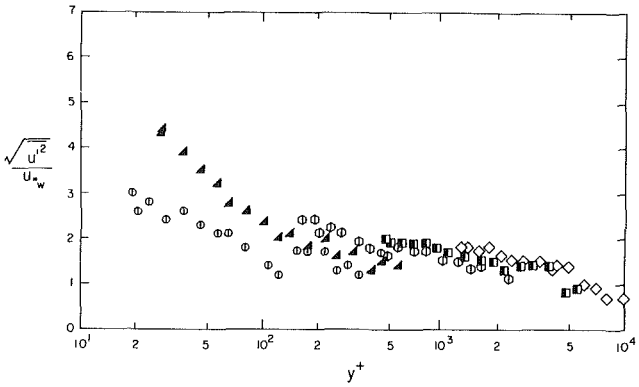

Fig. 7 Normalized root-mean-square turbulent fluctuations of the horizontal velocity versus y^+ (symbols same as in Fig. 1)

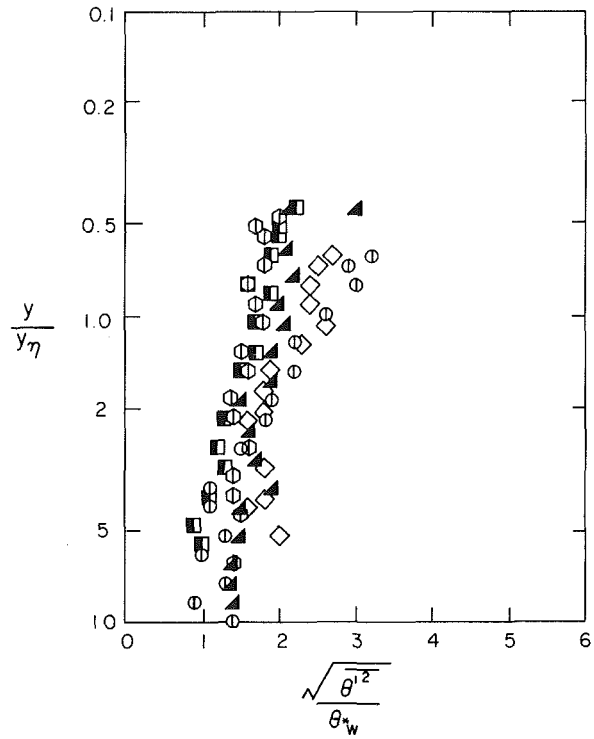

Fig. 8 Normalized root-mean-square water temperature (symbols same as in Fig. 1)

From Figs. 4 and 5 it is also obvious that, at any wind speed for which there are surface water waves, the horizontal and vertical turbulent fluctuations of the velocity are roughly equal

[although generally $(\overline{v'^2})^{1/2} < (\overline{u'^2})^{1/2}$]

at all depths when y_η is used for normalization. In a normal boundary layer over a smooth or rough solid wall,

$$(\overline{v'^2})^{1/2} < (\overline{u'^2})^{1/2}$$

and the ratio

$$(\overline{v'^2})^{1/2}/(\overline{u'^2})^{1/2}$$

decreases as the surface is approached (Hinze [10]). Exactly these trends appear in the present turbulent data for the lowest wind speeds *where the interface is smooth* if the law-of-the-wall coordinate y_w^+ is used in lieu of y/y_η. *When the surface is rough*, the presence of the moving wave forms makes it difficult to approach close enough to the surface with probes to observe if the expected decrease in

$$(\overline{v'^2})^{1/2}/(\overline{u'^2})^{1/2}$$

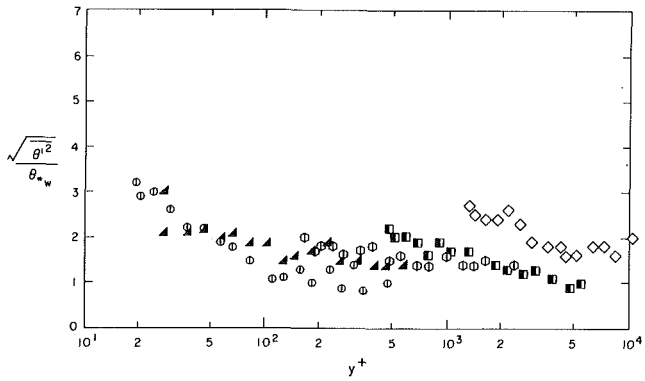

Fig. 9 Normalized root-mean-square water temperature versus y^+ (symbols same as in Fig. 1)

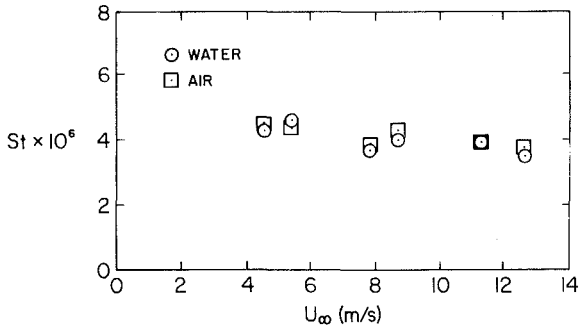

Fig. 10 Comparison of total flux across the interface as measured in the air and in the water

occurs very near the interface. The presence of the surface waves appears, however, to reduce the level of anisotropy in the horizontal and vertical components (the third component was, of course, not measured in our work).

Figures 6 and 7 serve to illustrate the penetration of the wave action with wind speed. As expected, at the lowest wind speed there are essentially no wave-induced fluctuations so

$$(\overline{\tilde{u}^2})^{1/2} << (\overline{u'^2})^{1/2}$$

For $U_\infty = 3.5$ m/s, the fluctuating intensities are about equal at the data points nearest the interface (i.e., for $y_w^+ < 100$). For greater U_∞ values, the maximum

$$(\overline{\tilde{u}^2})^{1/2} \text{ exceeds the maximum } (\overline{u'^2})^{1/2}$$

by a factor of approximately 2. Of course, as y_w^+ increases, the wave-induced quantities decrease very rapidly.

The normalized root-mean-square water temperature fluctuations are plotted in Figs. 8 and 9. There are no obvious trends in the values with wind speed for those cases where waves are measurable. The rapid increase in

$$(\overline{\theta'^2})^{1/2}/\theta_{*_w}$$

with decreasing depth for the 1.6 m/s case reflects typical smooth solid wall boundary layer behavior. As expected, the remaining data for

$$(\overline{\theta'^2})^{1/2}/\theta_{*_w}$$

collapse essentially to a single curve when plotted versus y_w^+ (Fig. 9), which further indicates typical boundary layer behavior within the water surface layer.

The total heat flux into the air is the sum of latent, sensible, and radiative components,

$$Q_{T_a} = Q_L + Q_S + Q_R$$

and should equal the single-phase heat transport, $Q_{T_w} = \rho_w c_{p_w} u_{*_w} \theta_{*_w}$, through the water surface layer. Only those data sets for which mean temperature and mean water-vapor concentration profiles were measured in the air could be used in these calculations. Q_S and Q_L were calculated using values of θ_{*_a} and q_{*_a} determined from the temperature and water-vapor concentration profiles, respectively; Q_R was estimated at 150 w/m^2 according to the results of Miller et al. [11]. The results, in the form of a water, heat-transfer Stanton number (based on free-stream wind speed U_∞, and the bulk water/free-stream air temperature difference, $\tilde{\theta}_B - \tilde{\theta}_\infty$) are given in Fig. 10. The agreement is very good.

Conclusions

The results and conclusions are summarized as follows:

1 Mean velocity and temperature profiles plotted in u^+, y^+ coordinates behave in a similar fashion on both sides of the air-water interface. Velocity profiles show the effects of increasing roughness with wind speed. The temperature profiles for $U_\infty \geq 3$ m/s fall approximately on one correlation (albeit a different one for the air and for the water). This confirms the conclusion of Street et al. [3], viz, that both in the air and in the water, the mechanism of momentum transfer is affected by surface roughness changes, but the mechanism of heat transfer is not (except for waveless surfaces).

2 Total heat flux measurements in the air and the water are in agreement, confirming an ability to predict air and water fluxes from knowledge of only one of them.

3 When viewed in standard boundary-layer wall coordinates, the purely turbulent fluctuations of temperature and velocity behave in a manner generally consistent with flow in boundary layers over solid surfaces.

Acknowledgment

This material is based on work supported by the National Science Foundation under Grant ENG-79-01176 from the Heat Transfer Program, Engineering Division. The authors are grateful, as well, to the reviewer who asked what fraction of the velocity profile data was taken within the wave boundary layer and whether wave affects caused the flattened profiles.

References

1 Howe, B. M., Chambers, A. J., and Street, R. L., "Heat Transfer at a Mobile Boundary," *Advances in Heat Mass Transfer at Air-Water Interfaces*, ASME, 1978, pp. 1-10.

2 Miller, A. W., Jr., and Street, R. L., "On the Existence of Temperature Waves at a Wavy Air-Water Interface," *Journal of Geophysical Research*, Vol. 83, 1978, pp. 1353-1365.

3 Street, R. L., Wang, C. S., McIntosh, D. A., and Miller, A. W., Jr., "Fluxes Through the Boundary Layers at an Air-Water Interface: Laboratory Studies," *Turbulent Fluxes through Sea Surfaces, Wave Dynamics, and Predictions*, eds. Favre and Hasselmann, 1978, pp. 99-120.

4 Bye, J., "The Wave-Drift Current," *Journal of Marine Research*, Vol. 25, 1967, pp. 95-102.

5 Csanady, G. T., "Turbulent Interface Flows," *Journal of Geophysical Research*, Vol. 83, 1978, pp. 2329-2342.

6 Csanady, G. T., "The 'Roughness' of the Sea Surface in Light Winds," *Journal of Geophysical Research*, Vol. 79, 1974, pp. 2747-2751.

7 McIntosh, D. A., Street, R. L., and Hsu, E. Y., "Turbulent Heat and Momentum Transfer at an Air-Water Interface: The Influence of Surface Conditions," Department of Civil Engineering, T.R. No. 197, Stanford University, 1975.

8 Ueda, H., Moller, R., Komori, S., and Mizushina, T., "Eddy Diffusivity Near the Free Surface of Open Channel Flow," *International Journal of Heat and Mass Transfer*, Vol. 20, 1977, pp. 1127-1136.

9 Kader, B. A., and Yaglom, A. M., "Heat and Mass Transfer Laws for Fully Turbulent Wall Flows," *International Journal of Heat and Mass Transfer*, Vol. 15, 1972, pp. 2329-2351.

10 Hinze, J. O., *Turbulence*, 2nd ed., McGraw-Hill, New York, 1975.

11 Miller, A. W., Jr., Street, R. L., and Hsu, E. Y., "The Structure of the Aqueous Thermal-Sublayer at an Air-Water Interface," Department of Civil Engineering, T.R. No. 195, Stanford University, 1975.

12 Benilov, A. Y., Kousnetsov, O. A., and Panin, G. N., "On the Analysis of Wind Wave-Induced Disturbances in the Atmospheric Turbulent Surface Layer," *Bound.-Layer Met.*, Vol. 6, 1974, pp. 269-285.

APPENDIX A
SPECTRAL WAVE SEPARATION

One can define (as did Benilov et al. [12]) a quantity linearly related to the surface waves as the "wave" component,

$$\tilde{x} = L\eta$$

where L is a linear operator and

$$x = \bar{x} + \tilde{x} + x'$$

where x can be one of the variables u, uv, etc.; $\bar{x}$ is the average value and x' is the turbulent fluctuation. In the frequency domain for the case with two variables,

$$S_{xy}(f) = S_{\bar{x}\bar{y}}(f) + S_{x'y'}(f)$$

Here $S_{xy}(f)$ is the cross spectrum of x and y. Computationally

$$S_{\tilde{x}\tilde{y}} = \frac{S_{x\eta}(f) \cdot S^*_{y\eta}(f)}{S_{\eta\eta}(f)}$$

$S_{\eta\eta}(f)$ is the power spectrum of η, the wave height signal. Using this method, one can separate the wave and turbulence components of any quantity of interest. However, turbulent components which are correlated with the wave will be incorporated in and computed as part of the equivalent wave component and non-linear wave terms will show up in the turbulent component.

APPENDIX B
UNCERTAINTY ESTIMATES

An uncertainty analysis was performed and led to the following estimates (at 20:1 odds):

Parameter	Uncertainty	Instrument
Water		
u	± 0.2 mm/s ($U_\infty < 2$ m/s) ± 0.6 mm/s (2 m/s $< U_\infty <$ 5 m/s)	LDA
v	± 1.6 mm/s (5 m/s $< U_\infty$)	
θ	± 0.1°C	thermistor or radiometer-thermistor
$\theta_w y - \theta_B$	± 0.01°C	
	± 0.25 mm	–
u_s	$\pm 10\%$ ($U_\infty < 9$ m/s) $\pm 20\%$ ($U_\infty > 9$ m/s)	paper punchings
η	± 0.3 mm or 2 percent (whichever is larger)	wave height gage
$\overline{u'^2}, \overline{v'^2}, \overline{\theta'^2}$	± 18 percent	–
$\bar{u}^2, \bar{v}^2, \bar{\theta}^2$	± 13 percent	–
$\overline{v'\theta'}$	± 18 percent	–
Air		
$U_\infty, u, u*$	± 0.1 m/s ($U_\infty < 8$ m/s) ± 0.2 m/s (8 m/s $< U_\infty$)	pitot-static tube
θ	± 0.1°C	thermistor